photonics

MDPI

Article

Modification of Thermal Network Parameters for Aerial Cameras via Integrated Monte-Carlo and Least-Squares Methods

Yue Fan [1,*], Wei Feng [1], Zhenxing Ren [1], Bingqi Liu [1] and Dazhi Wang [2]

[1] College of Mechanical Engineering, Chengdu University, Chengdu 610106, China; fengwei@cdu.edu.cn (W.F.); renzhenxing@cdu.edu.cn (Z.R.); liubingqi@cdu.edu.cn (B.L.)
[2] Institute of Optics and Electronics, Chinese Academy of Sciences, Chengdu 610209, China; wangdazhi@ioe.ac.cn
* Correspondence: fanyue@cdu.edu.cn

Abstract: The precise thermal control of aerial cameras is crucial for the acquisition of high-resolution imagery, and an accurate temperature prediction is essential to achieve this. This paper presents a methodology for modifying thermal network models to improve the accuracy of temperature prediction for aerial cameras. Seven types of thermal parameters are extracted from the thermal network model, and a thermally sensitive analysis identifies eleven key parameters to streamline the processing time. Departing from traditional methods that rely on steady-state data, this study conducts transient thermal tests and leverages polynomial fitting to facilitate thorough parameter modification. To ensure data reliability, the Monte-Carlo algorithm is employed to explore the parameter spaces of key parameters, analyzing temperature errors. Subsequently, the Least-Squares method is utilized to obtain optimal estimates of the key parameter values. As a result, the updated model demonstrates significantly improved accuracy in temperature predictions, achieving a reduction in the maximum absolute error between the predicted and experimental results from 22 °C to 4 °C, and a lowering of the relative error from 33.8% to 6.1%. The proposed modification method validates its effectiveness in modeling and enhancing the precision of thermal network models for aerial cameras.

Keywords: aerial camera; thermal network model; parameter modification; Monte-Carlo algorithm; least-squares method

Citation: Fan, Y.; Feng, W.; Ren, Z.; Liu, B.; Wang, D. Modification of Thermal Network Parameters for Aerial Cameras via Integrated Monte-Carlo and Least-Squares Methods. *Photonics* **2024**, *11*, 641. https://doi.org/10.3390/photonics11070641

Received: 6 June 2024
Revised: 27 June 2024
Accepted: 2 July 2024
Published: 4 July 2024

1. Introduction

Aerial cameras, as precision optical instruments, require stringent machining and assembly tolerances, and exhibit remarkable sensitivity to their surrounding environment. Operating under intricate and dynamic conditions, temperature fluctuations play a crucial role in significantly affecting the imaging quality [1–4]. Therefore, a thermal optimization design is paramount for achieving high resolution and reliability in optical systems. This optimization heavily relies on accurate predictions of thermal characteristics derived from a thorough thermal analysis. However, the intricate internal structure of aerial imaging systems, coupled with the constantly fluctuating external thermal environment, poses significant challenges in thermal analysis and temperature calculations [5–8]. The lumped-parameter thermal network (LPTN) model, which leverages the analogies between heat transfer and electrical conduction processes, offers a practical and effective means for estimating the temperature of aerial cameras [9–11].

However, the development of a lumped-parameter thermal network (LPTN) model inherently involves approximations and assumptions that may introduce modeling inaccuracies. Differences in processing methods, surface characteristics, and the dynamic environmental conditions can create discrepancies between physical properties and the estimated parameter values. Additionally, accurately determining the contact heat transfer coefficient and convection heat transfer coefficient can be a challenging task, potentially

leading to inaccuracies in the thermal network model's parameter values. Consequently, it is crucial to refine the LPTN model to achieve more precise predictions of temperature distributions within aerial camera systems [12,13].

Numerous researchers have delved deeply into the correction of thermal networks pertaining to aerospace instruments. Toussaint et al. [14] initially proposed a systematic method for correcting satellite thermal network models, which was founded on experimental data from thermal balance tests. Shimoji et al. [15] further refined crucial parameters of the thermal network by utilizing statistical regression analysis. Weng and Papalexandris [16,17] leveraged the Least-Squares method to update the parameter values of thermal network models. Beck et al. [18] successfully applied the particle swarm optimization technique to adjust thermal model parameters, with a primary focus on linear conductivity. Torralbo et al. [19] employed the Jacobian matrix formulation along with the Moore–Penrose pseudo-inverse to effectively minimize parameter uncertainty within the thermal mathematical model. Cui et al. [20] introduced a thermal model updating method that utilized the Kriging model as a surrogate model to optimize the thermal design parameters of a solar spectrometer, rather than relying on direct iterations of finite element analysis. Li et al. [21] integrated Latin hypercube sampling with the coordinate rotation method to enhance the accuracy of the spacecraft's thermal analysis model.

Herrera and Sepúlveda [22] were the pioneers in applying the Monte-Carlo stochastic approximation method to satellite thermal analysis. Cheng et al. [23] successfully refined the thermal model of a thermally controlled satellite in ground test conditions by leveraging the Monte Carlo hybrid algorithm. Zhang et al. [24] corrected the sensitive parameters of a small satellite using the Monte-Carlo mixed method, which involved classification layer by layer. Shi et al. [25] developed a predictor-corrector Monte-Carlo method, resulting in more precise solutions for the thermal radiative transfer equations. Gómez et al. [26] developed a new method based on statistical error analysis and the Monte-Carlo method for an uncertainty calculation in spacecraft thermal control and design. Furthermore, Anglada et al. [27] presented the validation of the genetic algorithm to correlate thermal mathematical models of space vehicles. Garmendia et al. [28] examined the correlation of a small–medium-size thermal model of space instruments using genetic algorithms.

Nevertheless, there has been a paucity of research into the modification of thermal network models for aerial cameras, particularly when considering convective heat transfer. Furthermore, most existing thermal network corrections are based on experimental steady-state thermal data, which require a lengthy and costly testing period. Consequently, the amount of experimental data available to perform corrections for all thermal network parameters is often insufficient to meet the demands of the task.

The present study aims to refine the parameters of thermal network models for aerial cameras by employing a combined approach of the Monte-Carlo and Least-Squares methods. The objective is to enhance the precision of temperature predictions for aerial cameras, which will ultimately result in more accurate and dependable assessments of the thermal performance. Based on the initial thermal network model, seven distinct thermal parameters are derived from the thermal resistances. Subsequently, a thermally sensitive analysis is conducted to assess the impact of each parameter on the temperature distribution within the optical system, thereby facilitating the identification of critical parameters. Additionally, transient thermal tests are performed to gather experimental data for a comprehensive parameter modification procedure. To ensure data reliability, the Monte-Carlo algorithm is utilized to explore parameter spaces for temperature error analysis. Following this, the Least-Squares method is employed to determine optimal estimates for the key parameters. Subsequently, a comparative analysis is undertaken, whereby the results of the original model are contrasted with those of the modified model.

2. Thermal Network Model of the Aerial Camera

2.1. Introduction of the Aerial Camera

An experimental aerial camera, derived from the original prototype and integrated with the preliminary thermal control design, is proposed to streamline the computational process, as shown in Figure 1. The experimental aerial camera, hereafter referred to as the aerial camera, has rotational symmetry along the X-axis and has an external dimension of Φ173 mm × 258 mm. It consists of an optical window, three sets of lenses, a lens barrel, an inner frame, an outer frame, and a rear cover. In addition, an insulation cover is attached to the end of the lens to simulate the influence of heat flow from the CCD components.

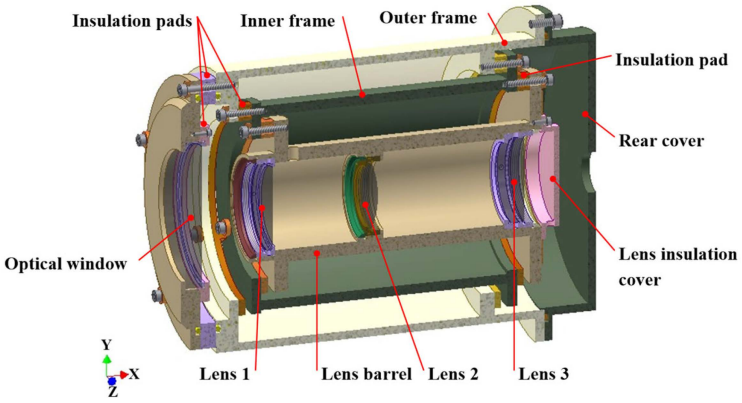

Figure 1. Cross section of the experimental aerial camera.

The aerial camera is installed in an unmanned aerial vehicle (UAV) that maintains a flight altitude of 9 km. During this flight, when the ground temperature is 20 °C, the ambient temperature surrounding the UAV reaches −38.5 °C. The optical window, oriented vertically towards the ground target, has its outer surface directly exposed to the external environment, leading to a rapid temperature drop and significant axial temperature difference. This variation directly affects the temperature of Lens 1, thereby influencing its performance and precision. Furthermore, the lens assembly and framework structure undergo substantial heat transfer through conduction, convection, and radiation, causing a rapid decrease in temperature levels and significant radial and axial temperature differences within the optical components.

2.2. Lumped-Parameter Thermal Network

The physical model is segmented into temperature units that maintain consistency in the temperature and heat flux. The thermal essence of each unit is focalized on its centroid, referred to as a node. Each node is distinctively characterized by its aggregated thermal attributes, encompassing the temperature and heat capacity, offering a holistic portrayal of its thermal behavior. To streamline the model, elements such as screws, apertures, and threads that minimally impact temperature are disregarded. Components with high thermal conductivity, like lens barrels and inner, and outer frames, are sparsely segmented into several nodes. In the instance of a lens with a confined thickness, the temperature variance along the radial axis is significantly greater than that along the axial axis. Therefore, the lens nodes should be densely allocated along the radial axis to guarantee precise thermal analysis. As the outer surface of the optical window is uniformly influenced by the external heat flux, resulting in minor temperature disparities in both radial and axial directions, it can be modeled as a solitary node. The original thermal network of the aerial camera is formulated by interconnecting nodes via thermal resistances, as depicted in Figure 2. In the figure, R_1–R_{43} are the conduction, contact, convection, or radiation thermal resistances between the nodes or the parallel or series connections of these thermal resistances, the arrows indicate the direction of the heat flow, and q_s is the external heat flux received by the outer surface of the optical window.

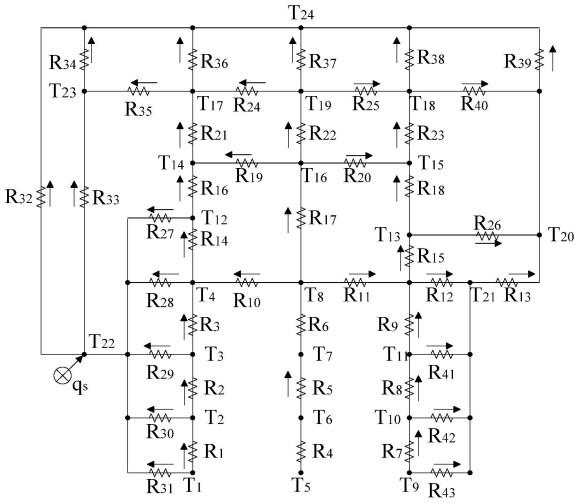

Figure 2. Lumped structure design of *R* and *T* parameters' network of the aerial camera.

2.3. Thermal Mathematical Model

The foundation of the thermal network mathematical model lies primarily in the analogous nature of heat transfer and conduction processes. Utilizing insights from Kirchhoff's current law and Ohm's law, the thermal balance equations for the nodes can be effectively established as [29]

$$C_i \frac{\mathrm{d}T_i}{\mathrm{d}\tau} = \sum_{j=1} D_{ij}(T_j - T_i) + \sum_{j} E_{ij}(T_j^4 - T_i^4) + \sum_{j} H_{ij}(T_j - T_i) + q_i \tag{1}$$

where C_i is the thermal capacity, T_i and T_j are the temperature of adjacent nodes, respectively, D_{ij}, E_{ij}, and H_{ij} are the thermal conduction, radiation, and convection coefficients, and q_i is the total heat source of the node, including the internal heat source and external heat flow into the node.

D_{ij}, E_{ij}, and H_{ij} can be represented by four types of thermal resistance, namely R_{cd}, R_{ct}, R_{cv}, and R_{rad}, which correspond to the conduction, contact, convection, and radiation thermal resistances, respectively. The calculation methods for the four types of thermal resistance are presented below.

A. Conduction thermal resistance

As the aerial camera is a rotationally symmetric structure, the conduction thermal resistance between nodes can be equated to the thermal resistance in a circular section [29], i.e.,

$$R_{\mathrm{cd}} = \frac{\ln(r_2/r_1)}{2\pi d\lambda} \tag{2}$$

where r_1 and r_2 are the radii of two adjacent nodes, respectively, d is the average thickness of the units where node 1 and node 2 are located, and λ is the thermal conductivity.

B. Contact thermal resistance

The contact thermal resistance can be expressed as

$$R_{\mathrm{ct}} = \frac{1}{h_{\mathrm{c}} A} \tag{3}$$

where h_{c} is the contact heat transfer coefficient, which can be given by the following empirical formula [29]:

$$h_{\mathrm{c}} = \frac{1}{L_{\mathrm{g}}}\left(\frac{A_{\mathrm{c}}}{A}\frac{2\lambda_A\lambda_B}{\lambda_A+\lambda_B} + \frac{A_{\mathrm{v}}}{A}\lambda_f\right) \tag{4}$$

where L_g is the thickness of the gap between the contact surfaces, A is the nominal contact area, A_c is the actual contact area, A_v is the uncontacted area, λ_A and λ_B are the thermal conductivities of the two contact parts, and λ_f is the thermal conductivity of the gas in the gap.

C. Convection thermal resistance

The convection thermal resistance in a concentric cylinder can be derived from the convective heat transfer coefficient as follows:

$$R_{cv} = \frac{1}{1.472\pi L\lambda_f}\left[\frac{g\mathrm{Pr}}{\alpha\nu\left(r_m^{-3/5}+r_n^{-3/5}\right)^5(0.861+\mathrm{Pr})}\right]^{-1/4}\left|\frac{T_m+T_n}{T_m-T_n}\right|^{0.25} \quad (5)$$

where L is the width of the rectangular cavity, λ_f is the thermal conductivity of the fluid, Pr is the Prandtl number, g is the gravitational acceleration, α is the thermal diffusion coefficient, ν is the kinematic viscosity, and r_m, r_n, T_m, and T_n are the radius and temperature of the hot surface and the cold surface, respectively.

D. Radiation thermal resistance

The radiation thermal resistance between concentric cylindrical surfaces can be written as

$$R_{rad} = \frac{\frac{1}{\varepsilon_i}+\frac{1-\varepsilon_o}{\varepsilon_o}\left(\frac{r_i}{r_o}\right)}{\sigma A_i(T_i^2+T_o^2)(T_i+T_o)} \quad (6)$$

where ε_i, ε_o, r_i, r_o, T_i, and T_o are the emissivity, radius, and temperature of the inner and outer surfaces, respectively, σ is the Steven–Boltsman constant, and A_i is the area of the inner surface.

The main thermophysical parameters that affect the thermal resistances are the thermal conductivity of the material, the contact heat transfer coefficient, the external and internal convective heat transfer coefficients, as well as the surface emissivity.

Table 1 presents seven types of thermal network parameters that are extracted from the thermal resistances. Due to the complexity of the camera structure, uncertainty in contact conditions, and fluctuations in the surface properties induced by environmental variations, the values of thermal network parameters are uncertain. These parameter values can be defined within a certain range based on empirical or theoretical values. Due to the limitations of the experimental conditions, it is unfeasible to simulate the flying convective environment on the exterior surface of the optical window. To align with the thermal testing parameters, it is assumed that the convection conditions on both the outer surface of the window and the exterior of the camera body are identical; specifically, both are subject to natural convection. The thermal resistances represented by the thermal network parameters are presented in Table A1, which is located in Appendix A.

Table 1. Thermal network parameters of the aerial camera.

Type	Parameter	Description	Initial Value	Range
Thermal conductivity ($W{\cdot}m^{-1}{\cdot}{}^{\circ}C^{-1}$)	k_1	Optical components	1.0	0.5–1.3
	k_2	Frame	160	8–200
Contact heat transfer coefficient ($W{\cdot}m^{-2}{\cdot}{}^{\circ}C^{-1}$)	k_3	Between lens and lens frame	5000	100–8000
	k_4	Between lens frame and lens barrel	4000	100–7000
Convective heat transfer coefficient of cylindrical structures ($W{\cdot}{}^{\circ}C^{-1}$)	k_5	Between lens barrel and inner frame	0.2	0.1–3.5
	k_6	Between inner frame and outer frame	0.3	0.1–4
Convective heat transfer coefficient of planar structures ($W{\cdot}m^{-2}{\cdot}{}^{\circ}C^{-1}$)	k_7	Between lens1 and optical window	7.8	2–50
	k_8	Between lens barrel and rear cover	6.7	2–50
	k_9	Between lens3 and lens insulation cover	8.2	3–50

Table 1. *Cont.*

Type	Parameter	Description	Initial Value	Range
External convective heat transfer coefficient ($W \cdot m^{-2} \cdot °C^{-1}$)	k_{10}	Between camera surface and environment	5	2–25
Emissivity	k_{11}	Lens barrel surface	0.8	0.5–1
	k_{12}	Frame surface	0.1	0.03–0.5
	k_{13}	Lens surface	0.9	0.3–1
	k_{14}	Optical window surface	0.4	0.2–1
Thermal resistance of insulation structure ($°C \cdot W^{-1}$)	k_{15}	Insulation structure of frames	50	10–50
	k_{16}	Insulation structure of the optical window	5	1–5

3. Sensitive Parameter Identification

To increase the efficiency of the model modification, it is essential to perform a sensitivity analysis of the thermal parameters. This analysis quantifies the influence of each parameter on the temperature distributions within the optical system and facilitates the identification of the key parameters that dominate the temperature variations.

The temperature fluctuation of the optical system resulting from variations of the thermal network parameters can be estimated by the following statistical equation:

$$\Delta T_i = \sqrt{\sum_{m=1}^{p} (S_m \cdot \Delta k_m)^2} \tag{7}$$

where T_i is the temperature of node i, Δk_m is the variation of the m-th thermal network parameter, p is the number of parameters related to T_i, and S_m is the sensitivity of the m-th thermal network parameter, which is defined as:

$$S_m = \frac{\partial T_i}{\partial k_m} \tag{8}$$

where k_m is the m-th thermal network parameter.

The analytical calculation of sensitivities can be a challenging task due to the complex nature of the thermal network equations. The numerical analysis method is used as a viable solution. The steady-state temperature variations of optical components are calculated by inserting parameter values within their respective ranges into the thermal network equations in response to changes in a single parameter. The sensitivity curves can then be derived by differentiating the temperature curves with respect to the respective parameters. It should be noted that when analyzing the sensitivity of a particular parameter, all other parameters are held at their initial values.

The sensitivity analysis results of partial parameters are indicated in Figure 3. By meticulously comparing the influence exerted by diverse parameters on the temperature of the optical system, along with analyzing the sensitivity curve, it is feasible to identify the crucial thermal network parameters that significantly impact the temperature distribution within the optical system of the aerial camera. The sensitivities of k_3, k_4, k_9, k_{11}, and k_{13} approximate zero, suggesting their minimal influence on the temperature distribution within the optical system. When revising the thermal network model, modifications are exclusively applied to the values of the crucial thermal network parameters, specifically k_1, k_2, k_5, k_6, k_7, k_8, k_{10}, k_{12}, k_{14}, k_{15}, and k_{16}. Meanwhile, the initial values of the insensitive parameters remain unchanged.

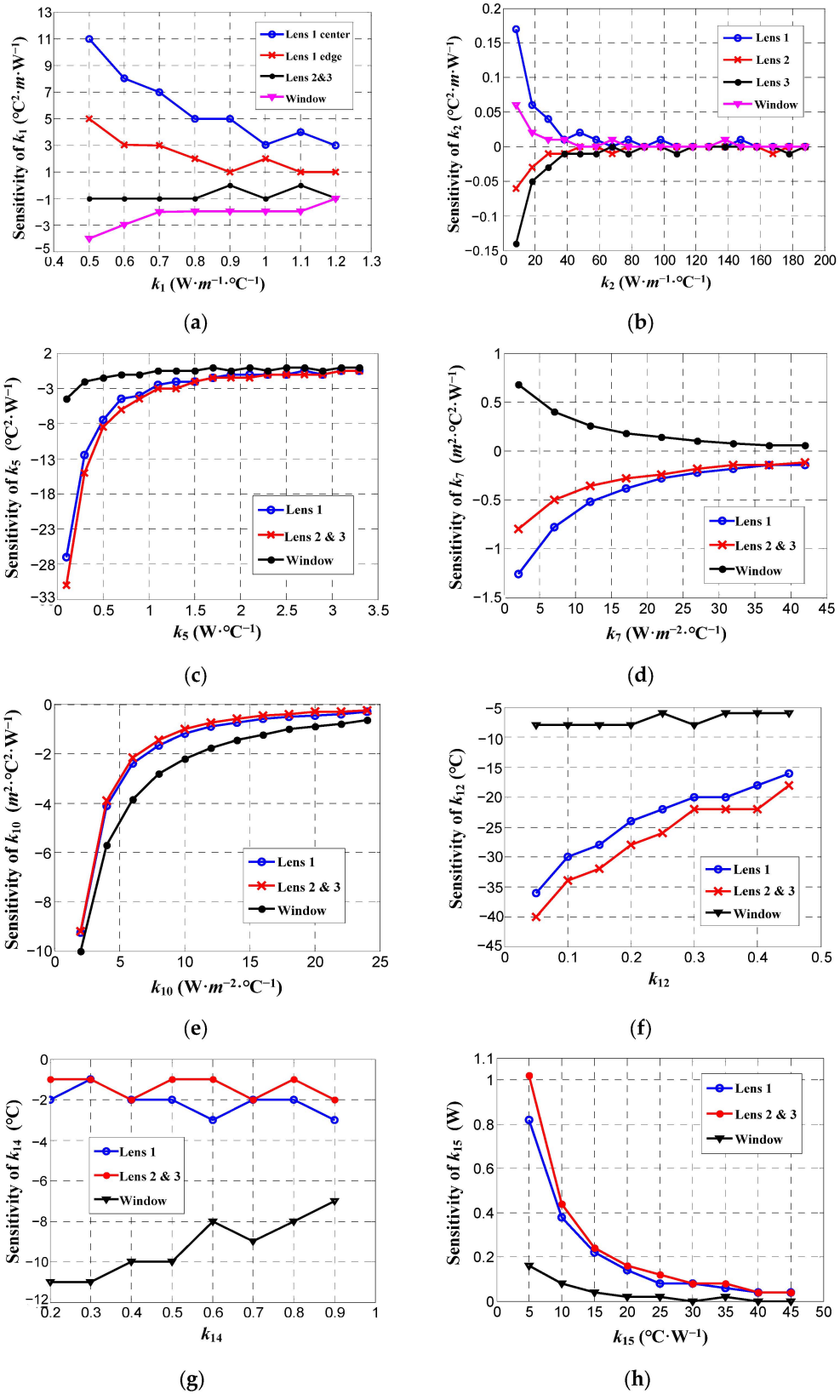

Figure 3. Sensitivity analysis of parameters in the thermal network model: (**a**) k_1; (**b**) k_3; (**c**) k_5; (**d**) k_7; (**e**) k_{10}; (**f**) k_{12}; (**g**) k_{14}; and (**h**) k_{15}.

4. Experimental Data Acquisition and Analysis

4.1. Transient Thermal Test

To overcome the limitation of limited data gathered from traditional steady-state thermal experiments, transient thermal tests have been conducted in this study. The objective is to gather more extensive and reliable experimental data, thereby facilitating comprehensive parameter modification. The transient thermal testing system comprises an aerial camera, a DC power supply, and a data acquisition and control module, as depicted in Figure 4. Inside the camera, heating films are wrapped onto the surface of the lens barrel, with varying heating conditions achieved by adjusting the power of each heating film. Temperature sensors are affixed at designated locations, corresponding to each node of the thermal network model, allowing for the real-time monitoring of temperature fluctuations at each node within the optical system. The DS18B20 is employed as the temperature sensor, offering 9-bit resolution. Its measurement accuracy within the range of −10 °C to 85 °C is ±0.5 °C, which fulfils the requirement of temperature measurement tolerance of ±1 °C.

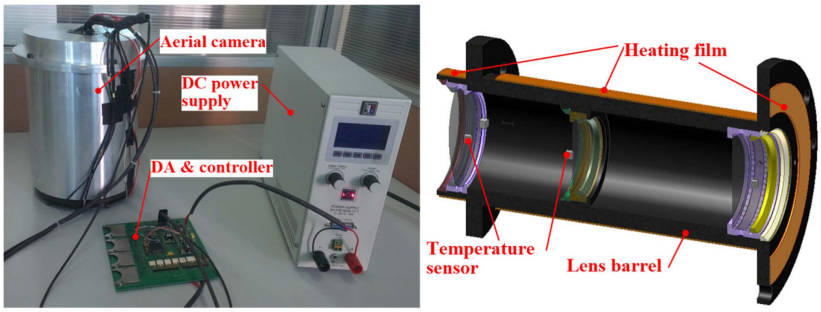

Figure 4. Setup of transient thermal tests.

Transient thermal tests are performed over 11 different heating conditions and the specific parameters for each condition are detailed in Table 2. Temperature data are collected at each node every 10 s, and using the *N*-order polynomial method, the discrete temperature data are accurately fitted to the temperature variation curves, as shown in Figure 5. This process generates sufficient temperature data to facilitate model modification.

Table 2. Operating parameters of transient thermal tests.

Condition Number	Voltage (V)	Initial Temperature of the Lens (°C)	Ambient Temperature (°C)	Heating Time (s)
1	8.6	30	20	10,900
2	10	21	16	6730
3	11	18	16	5170
4	12	20	17	3920
5	13	17	16	3140
6	14	19	16	2640
7	15	20	16	2610
8	16	22	20	1510
9	17	18	15	2310
10	18	21	19	1570
11	10	74	18	0

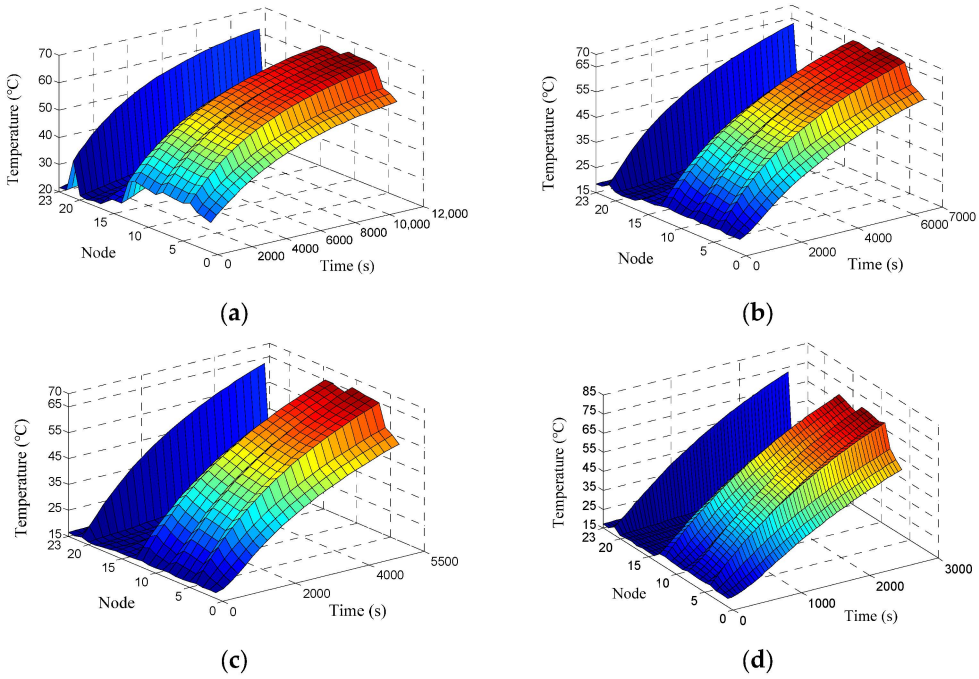

Figure 5. Fitting temperature curves of transient thermal testing data: (**a**) condition 1; (**b**) condition 2; (**c**) condition 3; and (**d**) condition 4.

4.2. Temperature Error Analysis

To enhance the precision of the thermal network model modification, evaluating the reliability of the experimental thermal data is crucial. Generally, discrepancies between the calculated and experimentally measured temperature values originate from several sources of error. These include deviations between the physical model and the mathematical model of the thermal network due to simplifications in the modeling process, calculation errors associated with numerical solutions, measurement inaccuracies exhibited by temperature sensors, and the imprecision of thermal network parameter values. Typically, the errors stemming from the first three factors can be roughly estimated through rigorous analysis. Therefore, this paper specifically delves into the discussion of temperature errors solely attributed to inaccuracies in thermal network parameters, with the aim of assessing the reliability of transient thermal testing data.

The Monte-Carlo method is utilized to analyze the transient temperature error. This approach involves establishing a probability model for each sensitive parameter. Following this, parameter values are randomly selected from the model and input into the thermal network equations. These equations are then solved, and the entire process is iterated numerous times. Through this iterative process, the mathematical expectation and mean square deviation of node temperatures are derived. The mathematical expectation signifies the most probable temperature value that would occur in the aerial camera, while the mean square deviation quantifies the potential temperature deviation.

The key parameters of the thermal network are regarded as random variables and presumed to exhibit a uniform distribution. Each parameter undergoes N rounds of sampling, and the simulation results show that when $N \geq 2000$, the parameters exhibit a uniform distribution. As a case study, the parameter spaces for the key parameters are randomly generated with a sampling number of 3000, adhering to their respective ranges of value, as depicted in Figure 6. Subsequently, the temperature variations of each node are calculated by feeding each set of parameters into the thermal network equations.

The temperature curve of a node is sampled at equal time intervals, and the average temperature of the node at the specific time point of τ_r is determined by

$$\overline{T(\tau_r)} = \frac{1}{N}\sum_{p=1}^{N} T_p(\tau_r) \tag{9}$$

where N is the sampling number of each key parameter.

In accordance with the Bessel formula, the standard deviation of the node temperature at the time point of τ_r is calculated by

$$\sigma_{T(\tau_r)} = \sqrt{\frac{\sum_{p=1}^{N}\left[T_p(\tau_r) - \frac{1}{N}\sum_{p=1}^{N} T_p(\tau_r)\right]^2}{N-1}} \tag{10}$$

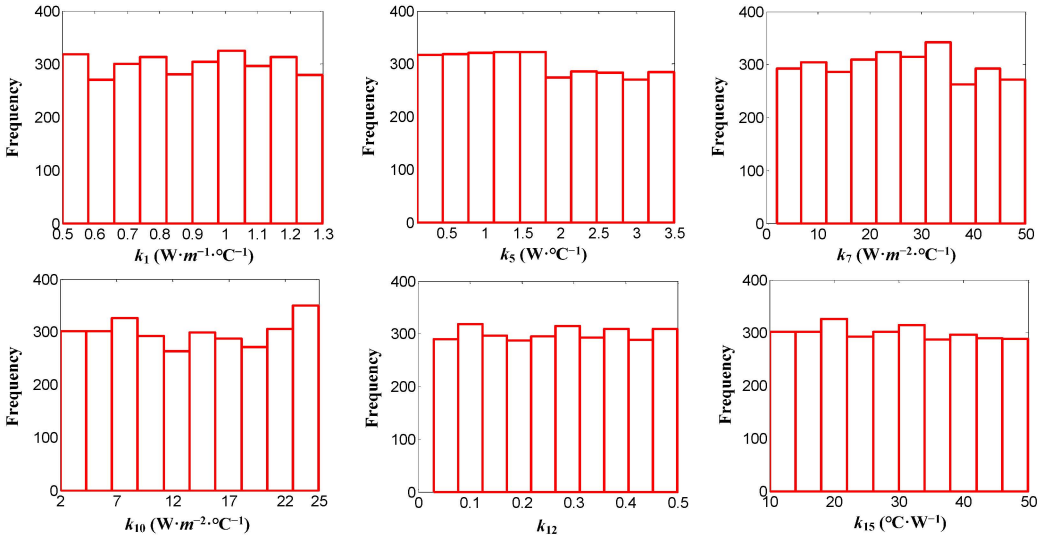

Figure 6. The parameter spaces for sensitive parameters with a sampling number of 3000.

Then, the transient temperature error of the node can be expressed by the root mean square of the temperature standard deviation at all sampling time points:

$$\delta T = \sqrt{\frac{\sum_{r=1}^{n_v}\sum_{p=1}^{N}\left[T_p(\tau_r) - \frac{1}{N}\sum_{p=1}^{N} T_p(\tau_r)\right]^2}{(N-1)n_v}} \tag{11}$$

where n_v is the sampling number for the calculated temperature curves.

The temperature error derived from the Equation (11) serves as an indicator of the potential temperature deviation at each node, thereby enabling an assessment of the reliability of the experimental temperature data.

The measured temperature curves under various heating conditions are sampled at equal time intervals with the same number of sampling points, and the root mean square error of the measured temperature values across all sampling points, relative to the average temperature, is subsequently calculated as follows

$$\delta T_s = \sqrt{\frac{\sum_{r=1}^{n_v}\left[T_s(\tau_r) - \overline{T_s}\right]^2}{n_v}} \tag{12}$$

where $T_s(\tau_r)$ is the measured temperature at sampling time point τ_r and $\overline{T_s}$ is the average temperature of all sampling points.

Figure 7 illustrates the calculated and measured temperature errors for the first four heating conditions. Upon the comparison of the calculated and measured temperature errors, it is evident that the measured temperature errors are generally smaller than the calculated ones, and this trend remains consistent across the other seven heating conditions, which suggests that the transient thermal test data exhibit high reliability and are well-suited for utilization in the modification of the thermal network model.

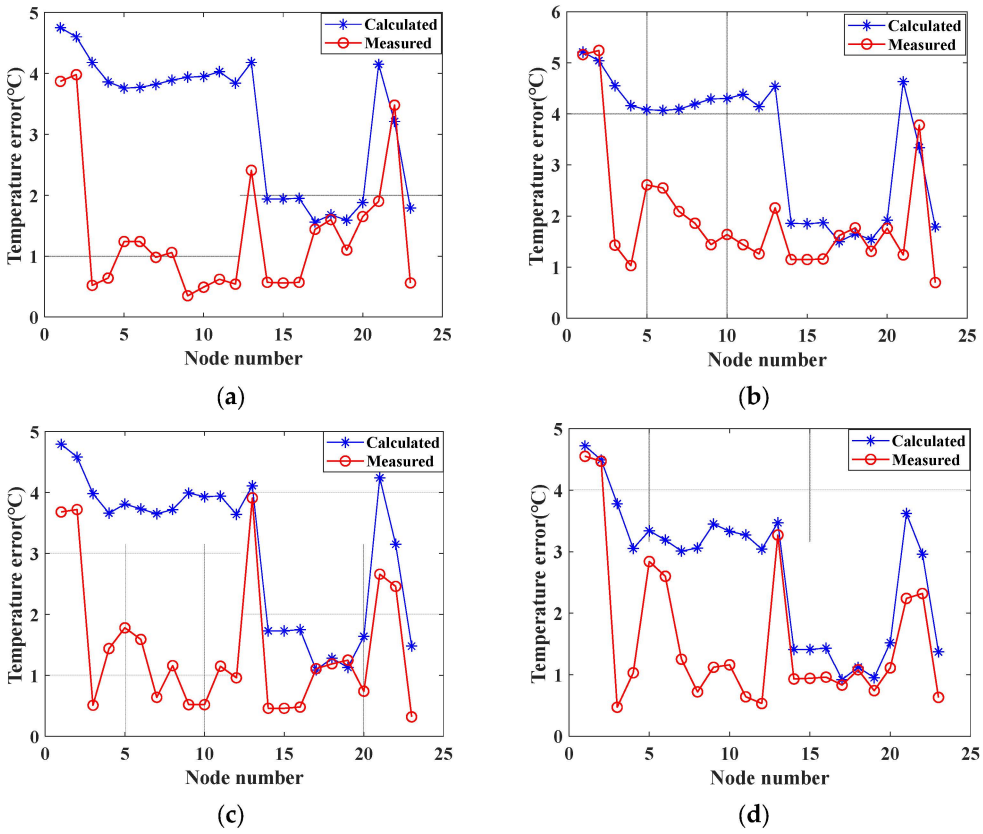

Figure 7. Comparison of calculated and measured temperature errors: (**a**) condition 1; (**b**) condition 2; (**c**) condition 3; and (**d**) condition 4.

5. Thermal Network Modification

5.1. Least-Squares Modification Process

The conventional approach to parameter modification using the least-squares method is to correct the values of the coefficients D_{ij}, E_{ij}, and H_{ij} within the thermal network equations. Although the physical sense of this approach is obvious, it requires the correction of numerous parameters, which is a significant computational and implementational challenge. In this study, transient thermal test data from aerial cameras are utilized to correct 11 key parameters, effectively reducing the number of parameters to be corrected by a factor of three and improving the efficiency of the correction process.

The specific process of using the least-squares method to correct the parameters of the thermal network model is as follows:

(1) The thermal balance equation of the aerial camera is written in the form of the residual equation as follows:

$$C_i \frac{dT_i}{d\tau} - \sum_j D_{ij}(T_j - T_i) - \sum_j E_{ij}(T_j^4 - T_i^4) - \sum_j H_{ij}(T_j - Ti) - q_i = U_i \quad (13)$$

where U_i is the residual heat of node i.

(2) Data processing of the thermal tests.

The temperature fitting curve of each node is sampled at regular time intervals, with the temperature sampling result of node i under the m-th heating condition expressed as a column vector ${T_i^{(m)}}_{(nm\times 1)}$, where n_m is the number of sampling points. This procedure guarantees that the temperature disparity between consecutive sampling points surpasses the measurement error. It is worth noting that the sampling points for each heating condition may differ, contingent on the temperature variation between adjacent sampling points. Subsequently, the consolidated sampling outcomes from 11 distinct heating conditions compile to form the temperature vector for node i, i.e.,

$$T_{i,11} = [{T_i^{(1)}}_{(n_1\times 1)}; {T_i^{(2)}}_{(n_2\times 1)}; \ldots; {T_i^{(11)}}_{(n_{11}\times 1)}] \tag{14}$$

where $T_{i,11}$ is a column vector comprising the $(n_1 + n_2 + \ldots + n_{11})$ temperature values.

For refining the thermal network model, if steady-state thermal test data are utilized, it becomes imperative to perform $(n_1 + n_2 + \ldots + n_{11})$ steady-state thermal tests. However, by leveraging transient thermal test data for correction, the requirement reduces to 11 transient thermal tests, significantly diminishing the overall number of thermal experiments.

The temperature polynomials of each node are differentiated with respect to time, resulting in the temperature change rate curves, as illustrated in Figure 8.

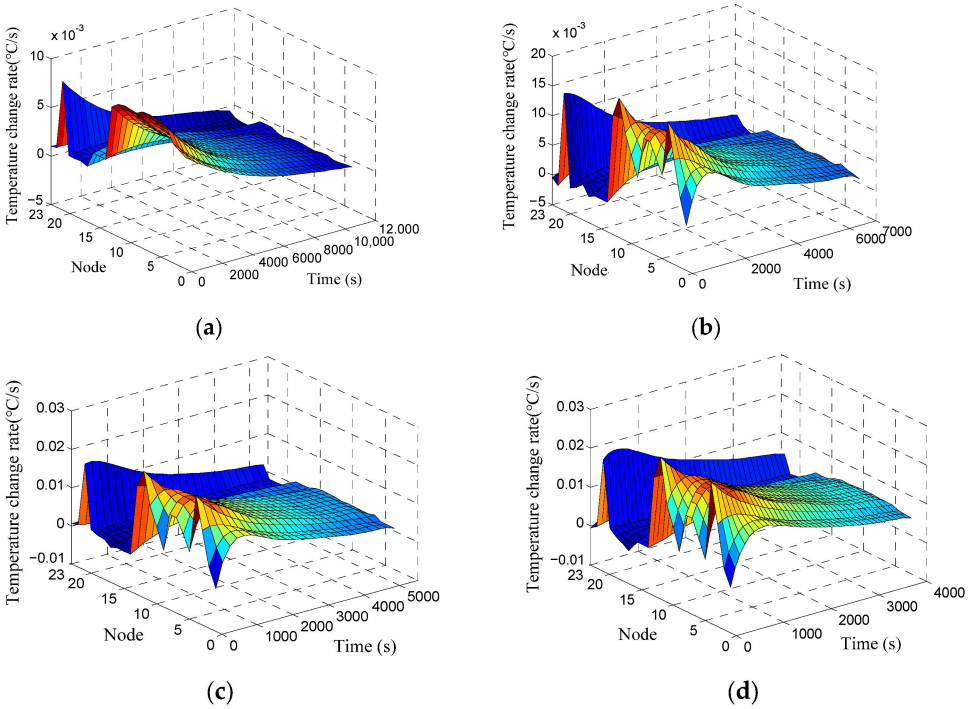

Figure 8. Temperature change rate curves of each node: (**a**) condition 1; (**b**) condition 2; (**c**) condition 3; and (**d**) condition 4.

The temperature change rate curve of the node is sampled at the same interval as the temperature curve, resulting in the temperature change rate vector $[\mathrm{d}T_i^{(m)}/\mathrm{d}\tau]_{(nm\times 1)}$ being obtained under the m-th heating condition. By combining the sampling results of the temperature change rate from 11 heating conditions, the temperature change rate vector of node i is derived by

$$\frac{\mathrm{d}T_{i,11}}{\mathrm{d}\tau} = \left[\frac{\mathrm{d}T_i^{(1)}}{\mathrm{d}\tau}_{(n_1\times 1)}; \frac{\mathrm{d}T_i^{(2)}}{\mathrm{d}\tau}_{(n_2\times 1)}; \ldots; \frac{\mathrm{d}T_i^{(11)}}{\mathrm{d}\tau}_{(n_{11}\times 1)}\right] \tag{15}$$

The heating power of node i is sampled at the same time interval, and the sampling results of the heating power from 11 working conditions are combined, resulting in the derivation of the heating power vector as follows

$$q_{i,11} = \left[q_i^{(1)}{}_{(n_1 \times 1)}; q_i^{(2)}{}_{(n_2 \times 1)}; \cdots ; q_i^{(11)}{}_{(n_{11} \times 1)} \right] \tag{16}$$

where $q_i^{(m)}{}_{(nm \times 1)}$ is the heating power vector of node i under the m-th heating condition, and $m = 1, 2, \ldots, 11$.

(3) By having the temperature vector, temperature change rate vector, and heating power vector of each node substituted into the residual equation of the corresponding node, the residual equations are derived as

$$\begin{aligned} &C_i \frac{\mathrm{d}T_{i,11}}{\mathrm{d}\tau} - \sum_j D_{ij}(T_{j,11} - T_{i,11}) - \sum_j E_{ij}(T_{j,11}^4 - T_{i,11}^4) \\ &- \sum_j H_{ij}(T_{j,11} - T_{i,11}) - q_{i,11} = U_i \end{aligned} \tag{17}$$

(4) The summation of the squared residuals pertaining to the heat of 23 nodes is obtained by

$$\Phi = \sum_{i=1}^{23} U_i^2 \tag{18}$$

Since D_{ij}, E_{ij}, and H_{ij} are all dependent upon the thermal network parameters, Φ is also a function of k_1 to k_{16}.

(5) Utilizing the principle of least squares, the cumulative squared deviation of the node heat Φ is minimized. By taking the derivative of the 11 key thermal network parameters, the subsequent system of equations is derived as

$$\frac{\partial \Phi}{\partial k_i} = 0, i = 1, 2, 5, 6, 7, 8, 10, 12, 14, 15, 16 \tag{19}$$

In the above equation system, the initial values of non-critical parameters are adopted, and a nonlinear system of equations comprising 11 key parameters is formulated. By solving the equations, the optimal estimate of the key parameters can be obtained.

5.2. Modification Results

Table 3 shows the optimal estimated values of the crucial thermal parameters derived from Equation (19), together with their original values and the corresponding percentage changes. It is noteworthy that k_5, k_6, k_7, k_8, and k_{10} exhibit considerable variations post-correction, suggesting that the convective heat transfer coefficients cannot solely rely upon theoretical formulations due to the fluid parameter uncertainties and irregular structural configurations. Additionally, remarkable alterations are also observed in the emissivity of the optical window surface, k_{14}, as well as the thermal resistance of insulation structures, k_{15} and k_{16}.

To determine the effectiveness of the model refinement, the initial and updated parameter values are introduced separately into the thermal network model for temperature calculation. Figure 9 displays the computed and observed transient temperature profiles for the central nodes of the lenses (nodes 1, 5, and 9) and the node positioned on the lens barrel (node 13), specifically during heating condition 1. Prior to thermal parameter refinement, it is evident that as the flight duration elongates, the temperature disparities between the calculated and measured temperatures substantially increase, attaining peak differences of 18 °C for the lens and 22 °C for the lens barrel. However, following the refinement process, considerable reductions in temperature deviations have been attained. Figure 10 portrays the transient temperature discrepancies between calculated and measured values post-correction of the thermal network model. It is discernible that the absolute errors remain within the range of −4 °C to 4 °C, accompanied by a substantial reduction in the

maximum absolute error by 18 °C, and a significant decline in the maximum relative error from 33.8% to 6.1%.

Table 3. Modified key parameter values of the thermal network model.

Parameters	Initial Value	Corrected Value	Change Percentage
k_1 (W·m^{-1}·°C^{-1})	1.0	0.92	−8.0%
k_2 (W·m^{-1}·°C^{-1})	160	148.8	−7.0%
k_5 (W·°C^{-1})	0.2	0.63	215.0%
k_6 (W·°C^{-1})	0.3	0.74	146.7%
k_7 (W·m^{-2}·°C^{-1})	7.8	10.4	33.3%
k_8 (W·m^{-2}·°C^{-1})	6.7	9.46	41.2%
k_{10} (W·m^{-2}·°C^{-1})	5	7.52	50.4%
k_{11}	0.8	0.76	−5.0%
k_{12}	0.1	0.09	−10.0%
k_{14}	0.4	0.56	40.0%
k_{15} (°C·W^{-1})	50	35.6	−28.8%
k_{16} (°C·W^{-1})	5	4.1	−18.0%

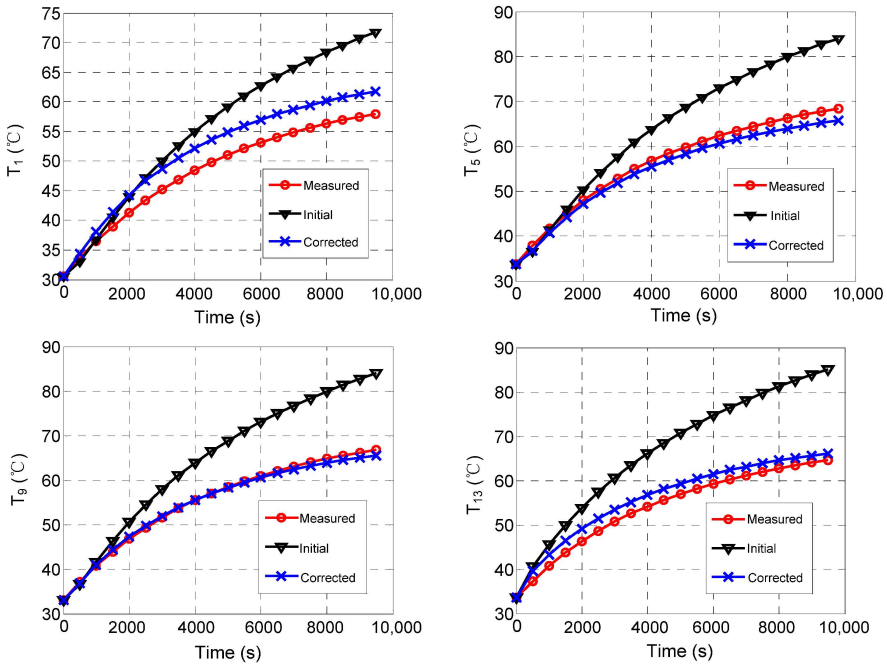

Figure 9. Comparative analysis of pre- and post-correction transient temperatures: calculated versus measured values.

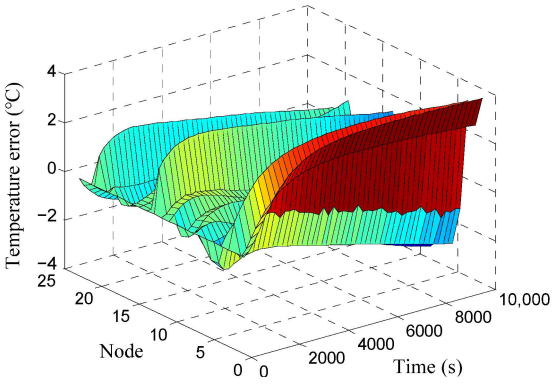

Figure 10. Transient temperature error curves: the deviations between calculated values refined by the least-square method and measured values.

5.3. Discussion

The parameter modification process and its outcomes demonstrate that the proposed methodology offers an efficient means of modeling the thermal network of aerial cameras. This methodology involves identifying the potential range of variations in thermal network parameters, considering factors like the geometric dimensions, fluid properties, and radiation angle coefficients during the modeling stage. For each thermal network parameter, an initial value is randomly selected from this range, and subsequently, the exact value is refined through the process of parameter correction.

As shown in Figure 10, after the modification, 90% of the deviations between calculated and measured values are within ±2 °C, which is a significant improvement in the temperature prediction accuracy compared to previous studies [18,23]. However, a residual error of up to 4 °C remains in lens 1, mainly due to the following sources of error:

(1) During the modeling process of the thermal network, the radiative heat transfer between the optical window and lens 1 is not considered, resulting in the heat from lens 1 not being fully transferred to the optical window. Consequently, the calculated temperature differs significantly from the measured value.

(2) Computation errors associated with the least-squares solutions. The least-squares solution depends on the experimental data and is very sensitive to errors in the experimental data.

Therefore, it is crucial to correct the structure of the thermal network prior to modifying its thermal parameters. Additionally, there is a need for further research into more robust methods for parameter correction within thermal networks.

6. Conclusions

In this paper, a comprehensive and systematic method for modifying the thermal network model is introduced, aimed at elevating the precision of temperature predictions and thermal performance acquisition for aerial cameras. A thermally sensitive analysis is performed among sixteen parameters, narrowing the focus to eleven critical thermal parameters, which enhances the efficiency of the model modification process. Transient thermal tests are conducted across eleven diverse heating conditions, resulting in the gathering of extensive experimental data to facilitate thorough parameter modification. This approach distinctively differs from conventional correction processes that rely solely on steady-state experimental data. To ensure the high reliability and suitability of the experimental data for parameter modification, a meticulous temperature error analysis is conducted utilizing the Monte-Carlo algorithm. Following this rigorous analysis, the Least-Squares method is employed to derive optimal estimates of the key parameters. Notably, due to the uncertainty of fluid parameters and structural factors, significant changes are observed in the values of convective heat transfer coefficients. Consequently, the temperature predicted by the updated model exhibits significantly improved accuracy. Specifically, the maximum absolute error is reduced from 22 °C to 4 °C, and the relative error is lowered from 33.8% to 6.1%.

The proposed modification method can be efficiently utilized to enhance the precision of thermal network models for aerial cameras. Simultaneously, it provides an effective methodology for the modeling process. This renders the simulation results derived from the mathematical models as valuable in exploring thermal performance and facilitating thermal design for such intricate systems.

In future research, the correction of the thermal network structure and the investigation of other optimization methods for thermal parameters will be considered to further improve the prediction accuracy of the thermal network model. In addition, based on the prediction of the thermal performance, research will be conducted on thermal control technology for aerial cameras.

Author Contributions: Y.F.: Conceptualization, Methodology, Investigation, Validation, Formal analysis, writing—original draft. W.F.: Conceptualization, Methodology. Z.R.: Data curation, writing—

review and editing. B.L.: Resources, Funding acquisition, Project administration. D.W.: Software. All authors have read and agreed to the published version of the manuscript.

Funding: This research was funded by the National Natural Science Foundation of China, grant number 42104174.

Institutional Review Board Statement: Not applicable.

Informed Consent Statement: Not applicable.

Data Availability Statement: The data are available from the corresponding author on reasonable request.

Conflicts of Interest: The authors declare no conflicts of interest.

Appendix A

Table A1. The thermal resistances represented by thermal parameters.

R_1	$16.8/k_1$	R_2	$11.7/k_1$	R_3	$4.9/k_1 + 2.4/k_2 + 1194.7/k_3 + 313.8/k_4$
R_4	$22.5/k_1$	R_5	$17.3/k_1$	R_6	$8.6/k_1 + 5.3/k_2 + 2144/k_3 + 458.5/k_4$
R_7	$13.5/k_1$	R_8	$8/k_1$	R_9	$2.7/k_1 + 1.7/k_2 + 684.8/k_3 + 235.2/k_4$
R_{10}	$43/k_2$	R_{11}	$59.7/k_2$	R_{12}	$10.3/k_2 + 482.3/k_4$
R_{13}	$\frac{1}{0.003k_8\left\|\frac{T_{21}-T_{20}}{T_{21}+T_{20}}\right\|^{0.28} + \frac{1.6\times10^{-10}}{1/k_{11}+1/k_{12}-1}(T_{21}^2+T_{20}^2)(T_{21}+T_{20})}$				
R_{14}	$23.6/k_2$	R_{15}	$17.9/k_2$	R_{16}	k_{15}
R_{17}	$\frac{1}{k_5\left\|\frac{T_8-T_{16}}{T_8+T_{16}}\right\|^{0.25} + \frac{1.9\times10^{-9}}{1/k_{11}+0.6(1/k_{12}-1)}(T_8^2+T_{16}^2)(T_8+T_{16})}$				
R_{18}	k_{14}	R_{19}	$35.2/k_2$	R_{20}	$35.2/k_2$
R_{21}	k_{15}	R_{22}	$\frac{1}{k_6\left\|\frac{T_{16}-T_{19}}{T_{16}+T_{19}}\right\|^{0.25} + \frac{3.4\times10^{-9}}{1.8/k_{12}-0.8}(T_{16}^2+T_{19}^2)(T_{16}+T_{19})}$		
R_{23}	k_{15}	R_{24}	$31.1/k_2$	R_{25}	$36/k_2$
R_{26}	$\frac{1}{0.01k_8\left\|\frac{T_{13}-T_{20}}{T_{13}+T_{20}}\right\|^{0.28} + \frac{4.8\times10^{-10}}{1/k_{11}+1/k_{12}-1}(T_{13}^2+T_{21}^2)(T_{13}+T_{21})}$				
R_{27}	$\frac{1}{0.002k_7\left\|\frac{\overline{T_1}-T_{22}}{\overline{T_1}+T_{22}}\right\|^{0.28} + \frac{4.8\times10^{-11}}{1/k_{11}+1/k_{14}-1}(T_{12}^2+T_{22}^2)(T_{12}+T_{22})}$				
R_{28}	$\frac{1}{0.001k_7\left\|\frac{\overline{T_1}-T_{22}}{\overline{T_1}+T_{22}}\right\|^{0.28} + \frac{4.4\times10^{-11}}{1/k_{11}+1/k_{14}-1}(T_4^2+T_{22}^2)(T_4+T_{22})}$				
R_{29}	$\frac{1}{0.001k_7\left\|\frac{\overline{T_1}-T_{22}}{\overline{T_1}+T_{22}}\right\|^{0.28} + \frac{3.6\times10^{-11}}{1/k_{13}+1/k_{14}-1}(T_3^2+T_{22}^2)(T_3+T_{22})}$				
R_{30}	$\frac{1}{7.4\times10^{-4}k_7\left\|\frac{\overline{T_1}-T_{22}}{\overline{T_1}+T_{22}}\right\|^{0.28} + \frac{2.3\times10^{-11}}{1/k_{13}+1/k_{14}-1}(T_2^2+T_{22}^2)(T_2+T_{22})}$				
R_{31}	$\frac{1}{2.3\times10^{-4}k_7\left\|\frac{\overline{T_1}-T_{22}}{\overline{T_1}+T_{22}}\right\|^{0.28} + \frac{7.3\times10^{-12}}{1/k_{13}+1/k_{14}-1}(T_1^2+T_{22}^2)(T_1+T_{22})}$				
R_{32}	$\frac{1}{0.005k_{10} + 2.9\times10^{-10}k_{14}(T_{22}^2+T_{24}^2)(T_{22}+T_{24})}$				
R_{33}	$11/k_1 + 4.6/k_2 + 1/(0.1 + 0.0015k_3)$				
R_{34}	$\frac{1}{0.02k_{10} + 1.2\times10^{-9}k_{11}(T_{23}^2+T_{24}^2)(T_{23}+T_{24})}$				
R_{35}	k_{16}	R_{36}	$\frac{1}{0.008k_{10} + 4.3\times10^{-10}k_{12}(T_{17}^2+T_{24}^2)(T_{17}+T_{24})}$		
R_{37}	$\frac{1}{0.08k_{10} + 4.6\times10^{-9}k_{12}(T_{19}^2+T_{24}^2)(T_{19}+T_{24})}$				
R_{38}	$\frac{1}{0.03k_{10} + 1.5\times10^{-9}k_{12}(T_{18}^2+T_{24}^2)(T_{18}+T_{24})}$				
R_{39}	$\frac{1}{0.05k_{10} + 2.6\times10^{-9}k_{12}(T_{20}^2+T_{24}^2)(T_{20}+T_{24})}$				
R_{40}	$40.9/k_2 + 89.4/k_4$				
R_{41}	$\frac{1}{0.001k_9\left\|\frac{\overline{T_9}-T_{21}}{\overline{T_9}+T_{21}}\right\|^{0.28} + \frac{3.7\times10^{-11}}{1/k_{12}+1/k_{13}-1}(T_{11}^2+T_{21}^2)(T_{11}+T_{21})}$				
R_{42}	$\frac{1}{7\times10^{-4}k_9\left\|\frac{\overline{T_9}-T_{21}}{\overline{T_9}+T_{21}}\right\|^{0.28} + \frac{2.6\times10^{-11}}{1/k_{12}+1/k_{13}-1}(T_{10}^2+T_{21}^2)(T_{10}+T_{21})}$				
R_{43}	$\frac{1}{2\times10^{-4}k_9\left\|\frac{\overline{T_9}-T_{21}}{\overline{T_9}+T_{21}}\right\|^{0.28} + \frac{7.8\times10^{-12}}{1/k_{12}+1/k_{13}-1}(T_9^2+T_{21}^2)(T_9+T_{21})}$				

References

1. Liu, W.; Ding, Y.; Wu, Q.; Jia, J.; Guo, L.; Wang, L. Thermal analysis and design of the aerial camera's primary optical system components. *Appl. Therm. Eng.* **2012**, *38*, 40–47. [CrossRef]

2. Jakel, E.; Erne, W.; Soulat, G. The thermal control system of the Faint Object Camera/FOC. In Proceedings of the AIAA, 15th Thermophysics Conference, Snowmass, CO, USA, 14–16 July 1980; p. 1501.
3. Yang, H.; Yuan, G.; Pan, J.; Zhou, D. Environmental Stability Design of the Aerial Mapping Camera Based on Multi-Dimensional Compound Structure. *Sensors* **2023**, *23*, 4421. [CrossRef] [PubMed]
4. Li, Y.; Yuan, G.; Xie, X.; Dong, L.; Yin, L. Multilayer thermal control for high-altitude vertical imaging aerial cameras. *Appl. Opt.* **2022**, *61*, 5205–5214. [CrossRef] [PubMed]
5. Liu, F.; Cheng, Z.; Jia, P.; Zhang, B.; Hu, R. Impact of thermal control measures on the imaging quality of an aerial optoelectronic sensor. *Sensors* **2019**, *19*, 2753. [CrossRef] [PubMed]
6. Liu, W.; Shen, H.; Xu, Y.; Song, Y.; Li, H.; Jia, J.; Ding, Y. Developing a thermal control strategy with the method of integrated analysis and experimental verification. *Optik* **2015**, *126*, 2378–2382. [CrossRef]
7. Cheng, Z.; Sun, L.; Liu, F.; Liu, X.; Li, L.; Li, Q.; Hu, R. Engineering design of an active–passive combined thermal control technology for an aerial optoelectronic platform. *Sensors* **2019**, *19*, 5241. [CrossRef] [PubMed]
8. Gao, Y.; Zhang, B.; Chen, L.; Xu, B.; Gu, G. Thermal design and analysis of the high resolution MWIR/LWIR aerial camera. *Optik* **2019**, *179*, 37–46. [CrossRef]
9. Edeson, R.L.; Shaughnessy, B.M.; Whalley, M.S.; Burke, K.; Lucas, J. The mechanical and thermal design and analysis of the VISTA infrared camera. In *Modeling and Systems Engineering for Astronomy*; SPIE: Glasgow, UK, 2004; pp. 508–519.
10. Fan, Y.; Liang, W.; Ma, W. Thermal design of the optical system in an aerial camera. *Opt. Electron. Eng.* **2013**, *40*, 51–58.
11. Xue, Z.; Wang, C.; Yu, Y.; Wang, P.; Zhang, H.; Sui, Y.; Li, M.; Luo, Z. Integrated optomechanical analyses and experimental verification for a thermal system of an aerial camera. *Appl. Opt.* **2019**, *58*, 6996–7005. [CrossRef]
12. Ishimoto, T.; Pan, H.M. Thermal network optimization techniques. In Proceedings of the 5th Thermophysics Conference, Los Angeles, CA, USA, 29 June–1 July 1970; p. AIAA-70-821.
13. Li, Y.H.; Yang, B.Y.; Wu, Y.N.; Zhang, Q.; Tang, X. Research on Parameters Calibration Method for Thermal Model of Satellite Optical Mechanical Load. *Acta Aeronaut. Astronaut. Sin.* **2023**, *420*.
14. Toussaint, M. Verification of the Thermal Mathematical Model for Artificial Satellite: A New Test Philosophy. In Proceedings of the AIAA, 2nd Thermophysics Specialist Conference, New Orleans, LA, USA, 17–20 April 1967; p. 304.
15. Shimoji, S.; Oshima, K. A new thermal network optimization method by the statistical regression analysis. In Proceedings of the 2nd AIAA/ASME Thermo-Physics and Heat Transfer 5th Thermophysics Conference, Palo Alto, CA, USA, 24–27 May 1978; Volume 78-882, pp. 344–365.
16. Weng, J.; Pan, Z. A optimization method for spacecraft thermal network and its coefficients. *Chin. Space Sci. Technol.* **1995**, *4*, 10–14.
17. Papalexandris, M.V.; Milman, M.H. Active control and parameter updating techniques for nonlinear thermal network models. *Comput. Mech.* **2001**, *27*, 11–22. [CrossRef]
18. Beck, T.; Bieler, A.; Thomas, N. Numerical thermal mathematical model correlation to thermal balance test using adaptive particle swarm optimization (APSO). *Appl. Therm. Eng.* **2012**, *38*, 168–174. [CrossRef]
19. Torralbo, I.; Perez-Grande, I.; Sanz-Andres, A.; Piqueras, J. Correlation of spacecraft thermal mathematical models to reference data. *Acta Astronaut.* **2018**, *144*, 305–319. [CrossRef]
20. Cui, Q.; Lin, G.; Cao, D.; Zhang, Z.; Wang, S.; Huang, Y. Thermal design parameters analysis and model updating using Kriging model for space instruments. *Int. J. Therm. Sci.* **2022**, *171*, 107239. [CrossRef]
21. Li, S.; Chen, L.; Liu, S. Thermal analysis model optimization method based on Latin hypercube sampling and coordinate rotation method. *J. Therm. Stresses* **2023**, *46*, 857–870. [CrossRef]
22. Herrera, F.L.; Sepúlveda, A. Stochastic Approach to Spacecraft Thermal Control Subsystem. In Proceedings of the International Conference on Environmental Systems, Toulouse, France, 21–25 July 2000.
23. Cheng, W.; Liu, N.; Li, Z.; Zhong, Q.; Wang, A.; Zhang, Z.; He, Z. Application study of a correction method for a spacecraft thermal model with a Monte-Carlo hybrid algorithm. *Chinese Sci. Bull.* **2011**, *56*, 1407–1412. [CrossRef]
24. Zhang, J.Y.; Chang, H.P.; Wang, L.G. Optimization method for transient thermal analysis model of small satellite. *Chin. Space Sci. Technol.* **2013**, *4*, 24–30.
25. Shi, Y.; Xie, H. A predictor–corrector Monte Carlo method for thermal radiative transfer equations. *Ann. Nucl. Energy* **2024**, *197*, 110252. [CrossRef]
26. Gómez-San-Juan, A.; Pérez-Grande, I.; Sanz-Andrés, A. Uncertainty calculation for spacecraft thermal models using a generalized SEA method. *Acta Astronaut.* **2018**, *151*, 691–702. [CrossRef]
27. Anglada, E.; Garmendia, I. Correlation of thermal mathematical models for thermal control of space vehicles by means of genetic algorithms. *Acta Astronaut.* **2015**, *108*, 1–17. [CrossRef]
28. Garmendia, I.; Anglada, E. Thermal mathematical model correlation through genetic algorithms of an experiment conducted on board the International Space Station. *Acta Astronaut.* **2016**, *122*, 63–75. [CrossRef]
29. Incropera, F.; DeWitt, D.; Bergman, T.; Lavine, A. *Fundamentals of Heat and Mass Transfer*; Chemistry Industry Press: Beijing, China, 2009.